Coupled Flow, Thermal, and Structural Analysis of Aerodynamically Heated Panels

Earl A. Thornton*
Old Dominion University, Norfolk, Virginia
and
Pramote Dechaumphai†
NASA Langley Research Center, Hampton, Virginia

A finite-element approach for coupling flow, thermal, and structural analyses of aerodynamicaly heated panels is presented. The Navier-Stokes equations for laminar compressible flow are solved, together with the energy equation and quasistatic structural equations of the panel. Interactions between the flow, panel heat transfer, and deformations are studied for thin stainless steel panels aerodynamically heated by Mach 6.6 flow.

Nomenclature

A	= element area
c	= fictitious damping constant
c_v	= specific heat at constant volume
E_t	= fluid total energy
h	= panel thickness
ℓ	= panel length
$[M]$	= mass matrix
$[N(x,y)]$	= element interpolation functions
p	= fluid pressure
q_x, q_y	= heat fluxes
$\{R\}$	= load vector
T	= temperature
t	= time
Δt	= time step
U	= typical conservation variable
u,v	= flow velocity components, Eq. (2), or solid displacement components, Eq. (4)
x,y	= coordinate directions
ρ	= density
$\sigma_{xx}, \tau_{xy}, \sigma_{yy}$	= fluid stress components
$\sigma_x, \tau_{zy}, \sigma_y$	= solid stress components

Subscripts

I	= inviscid flux
V	= viscous flux
n	= time-step index

Superscript

n	= time-step index

Introduction

THERMAL/STRUCTURAL analysis methods have an important role in the design of high-speed flight vehicles that experience severe aerodynamic heating. Traditionally, the prediction of thermally induced deformations and stresses has been accomplished as a sequence of analyses. First, heating rates are predicted on aerodynamic surfaces using either empirical methods or computationally using finite-difference/volume methods. Then, the structural temperatures are determined using a network-type thermal analysis or, more recently, via a finite-element thermal analysis. Finally, structural deformations and stresses are computed by a finite-element analysis using temperatures as input data. This approach is generally effective and indeed has been used routinely in the design of flight vehicles exposed to severe thermal environments. However, this approach is recognized as having two shortcomings: 1) the sequence of analyses is relatively inefficient because the incompatible models used in the three analyses make data transfer difficult, and 2) the approach assumes that the heat transfer between the fluid and structure and thermally induced deformations have negligible effects on the aerodynamic heating. The effects of the heat transfer and deformations on the heating may be considerd by an iterative sequence of analyses, but the process is cumbersome and is usually not attempted.

Yet there exist design problems in which fluid/thermal/structural interactions are important. One example is metallic thermal protection systems tested in the Mach 7 8-ft High-Temperature Tunnel (HTT) at the NASA Langley Research Center.[1] The tests show that panels "bowed-up" into the flow to produce heating rates that are up to 1.5 times greater than flat-plate predictions. Aerothermal loads on spherical dome protuberances have been studied both computationally[2] and experimentally.[3] The computations and experiments show that heating rates are augmented on windward surfaces and that the increase in heating rates depends on the protuberance height compared to the boundary-layer thickness. The computational and experimental determination of the augmented heating rates was based on assumed surface configurations and neglects flow/structural deformation interactions.

A second example of important problems in which flow, thermal, and structural interactions are important is the scramjet engine structure for the national aerospace plane. Figure 1 shows the sidewalls and leading edge of the engine structure where interactions may be significant. The leading edge of the internally cooled scramjet fuel injection strut is an especially critical area.

Research is under way at the NASA Langley Research Center to improve the capabilities and efficiency of finite-element high-speed compressible flow analysis methods and to develop efficient coupling of finite-element fluid, thermal, and structural analyses. The focus of the research is the prediction of aerothermal loads, as well as the thermal/structural response of complex three-dimensional bodies. The research combines

Presented as Paper 87-0701 at the AIAA/ASME/AHS/ASEE 28th Structures, Structural Dynamics and Materials Conference, Monterey, CA, April 6-8, 1987; received May 19, 1987; revision received Sept. 23, 1987.

*Professor, Department of Mechanical Engineering and Mechanics. Associate Fellow AIAA.

†Aerospace Technologist, Aerothermal Loads Branch, Loads and Aeroelasticity Division. Member AIAA.

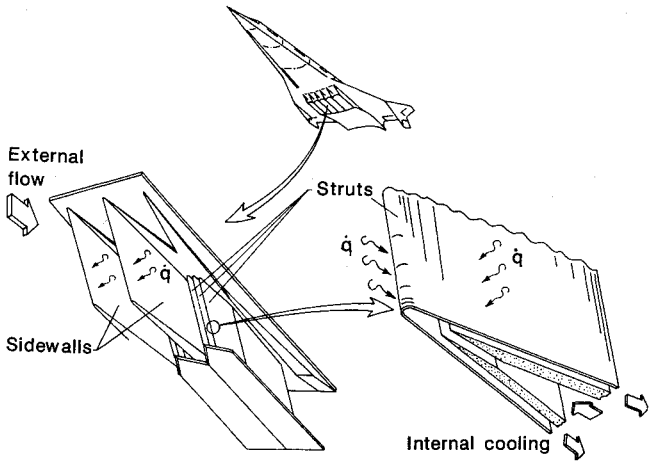

Fig. 1 Potential areas for fluid/thermal/structural interactions on aerospace plane scramjet engine structure.

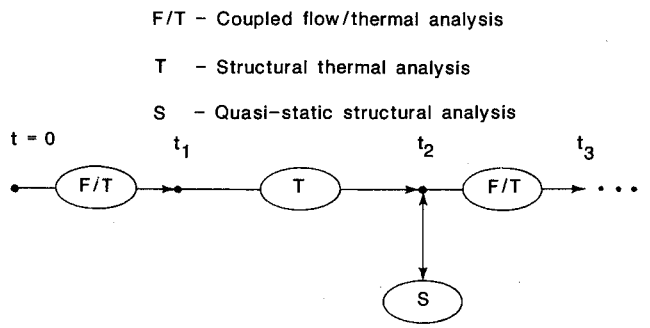

Fig. 2 Solution sequence for coupled flow / thermal / structural analysis.

analysis with experimental studies conducted in the 8-ft HTT at NASA Langley.

The purpose of this paper is to describe research in the coupling of flow, thermal, and structural analyses by the finite-element method for aerodynamically heated panels. The study of the interactions for panels is a preliminary, but important, step toward the objectives of analyzing more realistic structures, such as thermal protection systems and scramjet engine structures. The paper will bring together for the first time the solution of the Navier-Stokes equations for the prediction of aerodynamic heating and the solution for the associated thermal/structural equations by a single finite-element algorithm in one integrated vectorized program. Over the last few years, with this goal in mind, the authors and co-workers have developed the methodology to solve the separate problems. Initial progress in solving inviscid compressible flows by the finite-element method is described in recent papers.[4-6] Progress in solving viscous compressible flows is described in Ref. 7, and the application of the CFD algorithm to thermal/structural problems is described in Ref. 8.

The problem formulation will be described first; then the solution approach will be presented. The Taylor-Galerkin algorithm will be highlighted, followed by a presentation of the solution sequence for the coupled problem. Finally, numerical results for two coupled flow-panel interactions are presented and discussed.

Flow/Thermal/Structural Formulation

The fluid flow is described by the conservation of mass, momentum, and energy equations for a laminar flow of a perfect gas, assuming temperature-dependent viscosity and thermal conductivity. The thermal behavior of the panel is described by the conservation of energy equation, and the structural behavior is described by the quasistatic equations of motion for a solid. Radiation heat transfer from the panel to space is considered, assuming that the fluid is perfectly transparent. Thermal properties such as specific heat and thermal conductivity are assumed temperature-dependent. Large-strain displacement relations are used for the panel to permit large deformation, and nonlinear, temperature-dependent stress-strain relations are employed to permit plastic deformation. The equations for the fluid and solid are written in conservation form.

Fluid:

$$\frac{\partial\{U\}}{\partial t}+\frac{\partial\{E_I-E_V\}}{\partial x}+\frac{\partial\{F_I-F_V\}}{\partial y}=0 \tag{1}$$

where $\{U\}$ is a vector of the conservation variables for the fluid, $\{E_I\}$ and $\{F_I\}$ are inviscid flux components, and $\{E_V\}$ and $\{F_V\}$ are viscous flux components. These vectors are given by

$$\begin{aligned}\{U\}^T &= [\rho\ \rho u\ \rho v\ \rho E_t]\\ \{E_I\}^T &= [\rho u\ \rho u^2+puv\ (\rho E_t+p)u]\\ \{F_I\}^T &= [\rho v\ \rho vu\ \rho v^2+p\ (\rho E_t+p)v]\\ \{E_V\}^T &= [0\ \sigma_{xx}\ \tau_{xy}\ (u\sigma_{xx}+v\tau_{xy}-q_x)]\\ \{F_V\}^T &= [0\tau_{xy}\ \sigma_{xy}\ (u\tau_{xy}+v\sigma_{yy}-q_y)]\end{aligned} \tag{2}$$

In the inviscid flux components, the pressure p is related to the total energy for a perfect gas, assuming a constant ratio of specific heats. The stress components are related to the velocity gradients, assuming the Stokes' hypothesis, and the heat fluxes are related to the temperature gradients by Fourier's law. The temperature-dependent viscosity is computed from Sutherland's law, and the thermal conductivity is computed assuming a Prandtl number equal to 0.72.

Solid:

$$\frac{\partial\{U\}}{\partial t}+\frac{\partial\{E\}}{\partial x}+\frac{\partial\{F\}}{\partial y}=0 \tag{3}$$

where $\{U\}$ is a vector of the conservation variable for the solid; $\{E\}$ and $\{F\}$ are "flux" components for the solid. These vectors are given by

$$\begin{aligned}\{U\}^T &= [cu\ cv\ \rho c_v T]\\ \{E\}^T &= [-\sigma_x\ -\tau_{xy}\ q_x]\\ \{F\}^T &= [-\tau_{xy}\ -\sigma_y\ q_y]\end{aligned} \tag{4}$$

This coefficient c of the displacement components is a fictitious damping constant that is used to facilitate time marching to a steady-state quasistatic solution. The solid's stress components σ_x, τ_{xy}, and σ_y are related to the displacement gradients within the elastic range using generalized Hooke's law. In the plastic range, a modified elastic stiffness based on an effective strain is employed using the material's nonlinear uniaxial stress-strain is curve.[9] The solid's heat fluxes q_x and q_y are related to the temperature gradients by Fourier's law.

The sets of Eqs. (1) and (3) are solved, subject to appropriate boundary, interface, and initial conditions, for the fluid and solid. Flow boundary conditions correspond to supersonic/hypersonic flow; hence, all conservation variables are specified on inflow surfaces. On supersonic outflow surfaces, the finite-element formulation provides appropriate natural boundary conditions. Solid boundary conditions include either specified displacements or surface tractions. At the fluid/solid interface, flow velocity components are zero, but the fluid density and the

fluid/solid temperature are unknown. Continuity of temperature at the fluid/solid interface is imposed explicitly in the solution algorithm. A heat flux energy balance is imposed at the fluid/solid interface to account for the fluid/solid conduction heat fluxes and the emitted radiation heat flux. Initially, the flow is assumed uniform at freestream values; the solid is assumed undeformed and unstressed at room temperature.

Solution Approach

The solution approach solves Eqs. (1) and (3) using an explicit time-marching scheme, the Taylor-Galerkin algorithm, which has been described in previous papers.[4-8] Herein, the essential features of the algorithm are highlighted, and the solution sequence for the coupled problem is presented.

Taylor-Galerkin Algorithm

The basic concept of the Taylor-Galerkin algorithm is to use: 1) Taylor series expansions in time to establish recurrence relations for time marching, and 2) the method of weighted residuals with Galerkin's criteria to develop the finite-element matrix equations describing the spatial distribution of the dependent variables.

For simplicity, the finite-element formulation will be given for a single scalar equation,

$$\frac{\partial U}{\partial t}+\frac{\partial E}{\partial x}+\frac{\partial F}{\partial y}=0 \tag{5}$$

where the variables U, E, and F are analogous to the corresponding vector quantities in Eqs. (1) or (3). Let $\{U\}^n$ denote the element nodal values of the flow variables (x,y,t) at time t_n. The time step Δt spans two typical times t_n and t_{n+1} in the transient response. The computation proceeds through two time levels, $t_{n+\frac{1}{2}}$ and t_{n+1}. At time level $t_{n+\frac{1}{2}}$, values for U, which are constant within each element, are computed explicitly. At time level t_{n+1}, the constant element values computed at the first time level are used to compute nodal values for U. In the time level t_{n+1} computations, element contributions are assembled to yield the global equations for nodal unknowns. The "mass" matrix for the resulting equations is approximately diagonalized to yield an explicit algorithm.

Time Level $t_n + \frac{1}{2}$

The constant element value $U_D^{n+\frac{1}{2}}$ is computed from

$$A\,U_D^{n+\frac{1}{2}}=\int_A[N]\,dA\,\{U\}^n-\frac{\Delta t}{2}\int_A\left[\frac{\partial N}{\partial X}\right]dA\,\{E\}^n-\frac{\Delta t}{2}\int_A\left[\frac{\partial N}{\partial y}\right]dA\,\{F\}^n \tag{6}$$

Quantities in braces, such as $\{E\}^n$, represent nodal values at time t_n.

Time Level t_{n+1}

The nodal values for a single element are given by

$$[M]\{U\}^{n+1}=[M]\{U\}^n+\Delta t\int_A\left[\frac{\partial N}{\partial X}\right]dA\,E(t_{n+\frac{1}{2}})+\Delta t\int_A\left[\frac{\partial N}{\partial Y}\right]dA\,F(t_{n+\frac{1}{2}})+\{R\}^{n+\frac{1}{2}} \tag{7}$$

where $\{R\}^{n+\frac{1}{2}}$ represents known boundary terms. The matrix $[M]$ is the consistent mass matrix; to produce an explicit algorithm, M is diagonalized. Following usual finite-element procedures, the element matrices given in Eq. (7) are then assembled to form system equations.

The two-time-level Taylor-Galerkin algorithm is conditionally stable, and the time step for the fluid flow must satisfy stability requirements based on the CFL condition and the Reynolds number. Artificial viscosity, the form due to Lapidus,[9] is used to reduce oscillations in the flow computations.

The time evolution of the flow and the solid thermal response is computed in a "time-accurate" fashion using the algorithm as described. The structural response is computed by time marching to steady state via a viscous relaxation procedure based on the Taylor-Galerkin algorithm.[8] To speed convergence of the quasistatic solution to steady state, the concept of accelerated viscous relaxation is employed.[11]

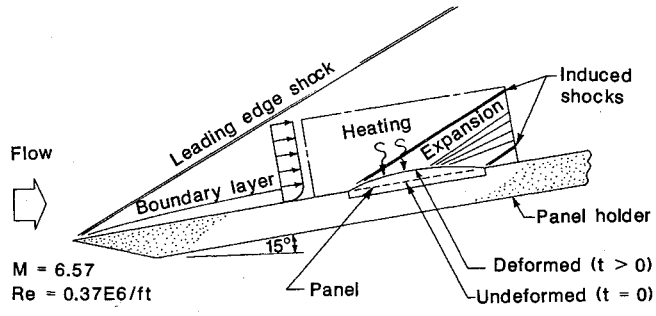

Fig. 3 Schematic diagram of experiment to validate flow/thermal/structural analysis.

Solution Sequence

Experimental and computational results for flows over panels show that the flow initially approaches steady state in a much shorter time than required for the panel to respond thermally and structurally. Typically, heating rates approach steady state in about a millisecond. A panel at this time remains virtually undeformed at temperatures only slightly higher than the initial temperature. After a few seconds, panel temperatures begin to rise appreciably, and significant deformations occur. During this time, thermal and deformation coupling effects alter the flowfield. The coupling effects continue to alter the flow and panel behavior until the panel reaches thermal equilibrium. Typically, panel thermal equilibrium is approached after 5-10 min of aerodynamic heating.

Based on this sequence of events, the solution sequence shown in Fig. 2 has been adopted. The solution sequence alternates between coupled flow and thermal analyses of the fluid/panel and thermal analysis of the panel. At selected times, temperatures of the panel are used to compute structural deformations. If significant, the structural deformations are used to define a new flow boundary.

Applications

Two applications are presented to illustrate the computational approach and investigate the coupled response of aerodynamically heated panels. The first application is a "flat" panel that, in the undeformed state, has zero angle of attack. The second application is a panel that, in the undeformed state, is oriented at 5 deg to the flow so that initially it forms a compression corner.

The flow conditions for the two applications correspond to test conditions in the 8-ft HTT at NASA Langley. A schematic of a proposed experiment to validate the flow/thermal/structural interaction analysis is shown in Fig. 3. In the proposed experiment, test panels are mounted in a panel holder with a sharp leading edge. The panel holder is oriented at 15 deg to the tunnel freestream so that an oblique leading-edge shock forms, producing the desired boundary layer on the panel holder. The figure schematically shows a panel supported in the panel holder in an initial flat orientation being heated at time $t = 0$ by the boundary-layer flow. After some time, the test panel deforms into the stream, altering the flow significantly by introducing local shocks, expansion regions, and shock boundary-layer interactions.

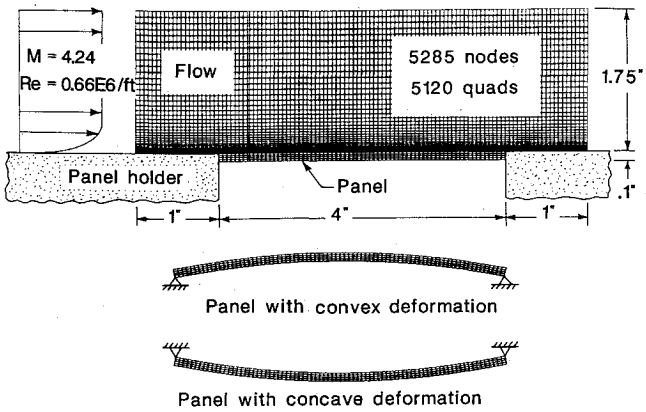

Fig. 4 Coupled flow/thermal/structural finite-element model and boundary conditions for flow over flat plate.

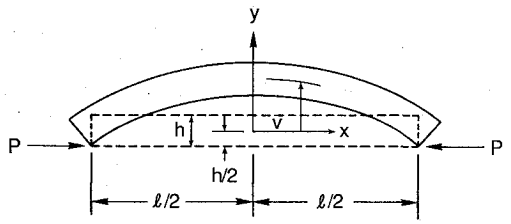

Fig. 5 Geometry of panel used in approximate beam-column structural analysis.

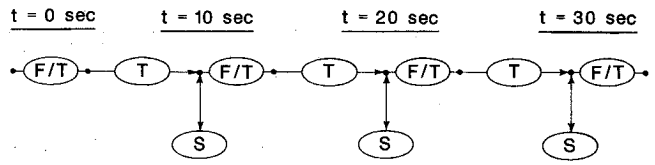

Fig. 6 Solution sequence for coupled flow/thermal/structural analysis of flow over flat plate.

Solution Validation

Because the solution approach is relatively complex and no experimental data are available to compare with the computational results, the finite-element computations were verified for early time by comparison with simplified solutions.

Aerodynamic Heating

The finite-element solution for the Navier-Stokes equations was validated in Ref. 7 by comparison with finite-difference solutions. For the undeformed panel shown in Fig. 3, the aerodynamic heating rate was compared with a boundary-layer solution to verify the finite-element results. For early times, the heating rate across the panel is nearly uniform and, as the panel is heated, the heating decreases as a result of the rise in panel temperatures. As an approximation during this time period, the heating rate may be estimated by

$$\dot{q}(t) = 0.026 - 0.00010t \text{ (BTU/in.}^2 - \text{s)} \tag{8}$$

The approximation will not be valid at later times because panel deformations will alter the flow so that the heating rate varies across the panel.

Panel Thermal Response

At early time, panel temperatures may be estimated by assuming 1) that energy losses at panel supports are negligible, 2) that radiation energy losses are negligible as a result of low panel temperature, 3) that no panel thickness temperature gradient is permissible for the present thin stainless steel panels because the Biot number (convection coefficient × panel thickness/conductivity) is small, about 0.02, and 4) that the panel specific heat may be assumed constant for small temperature changes. With these assumptions, a panel energy balance gives

$$\rho ch \frac{dT_a}{dt} = \dot{q}(t) \tag{9}$$

where T_a is the panel average temperature. Substituting Eq. (8) into Eq. (9) and integrating yields

$$T_a(t) = 1/\rho ch \cdot (0.026t - 0.00005t^2) + T_0 \tag{10}$$

where T_0 is the panel initial temperature.

Table 1 Temperature-dependent panel properties[a]

Property	a	b
ρ, lb = m/in.^{3}	0.28200	0
C_v, BTU/lb = m-°R	0.11162	0.36559×10^{-4}
k, BTU/s-in.-°R	0.12864×10^{-3}	0.11325×10^{-6}
ϵ, dimensionless	0.47577	0.70588×10^{-4}
α, 1/°R	0.62643×10^{-5}	0.35714×10^{-9}
E, lb = f/in.^{2}	0.35346×10^{8}	-0.98366×10^{4}

[a]Material properties are assumed to vary linearly with temperature in the form $a + bT$, where T is in °R.

Panel Structural Response

At early time, the panel's structural response may be approximated by beam-column theory.[12] The theory assumes that deformations are small, shear effects are neglected and, for cylindrical bending, the beam's flexural rigidity is $D = Eh^3/12(1 - \nu^2)$, where E is the modulus of elasticity and ν Poisson's ratio. Because panel temperatures are uniform, there are no thermal bending moments. Calculations show that deformations caused by transverse aerodynamics pressure are negligibly small compared to thermal deformations. For the panel geometry shown in Fig. 5, beam-column theory was used to derive an approximate solution for the panel deflection $v(x)$ and the panel bending stress $\sigma_x(x,y)$. The deflection is given by

$$v(x) = (h/2)\,(\cos\lambda x/2 - 1) \tag{11}$$

where $\lambda = \sqrt{P/D}$, and the axial constraint force P is computed from

$$\frac{P\ell}{hE} + \frac{h^2}{2}\lambda \tan\left(\frac{\lambda\ell}{2}\right) + \frac{h^2}{8}\frac{P}{D} \times \left(\frac{\ell}{2} - \frac{\sin\lambda\ell}{2\lambda}\right) \Big/ \cos^2\frac{\lambda\ell}{2} - \alpha\Delta T\ell = 0 \tag{12}$$

where $\Delta T = T_a - T_0$. Equation (10) results from imposing the condition that the panel supports are immovable. The panel stresses according to beam-column theory are

$$\sigma_x = -\frac{P}{h} + \frac{6P}{h^2}\frac{\cos\lambda x}{\cos\lambda\ell/2}y \tag{13}$$

where y is defined in Fig. 5.

Flat Panel

The finite-element model and boundary conditions for the flat panel are shown in Fig. 4. The test panel is 4 in. long, has a thickness of 0.1 in., and is made for AM-350 stainless steel. Temperature-dependent properties for the panel are tabulated in Table 1. The flow conditions and profiles at the left boundary

of the computational domain were determined from a boundary-layer solution for the panel holder shown in Fig. 3. The computational domain is modeled with a finite-element mesh of 5285 nodes and 5120 quadrilateral elements. About 95% of the nodes lie in the flow domain. The mesh is graduated normal to the panel to produce high resolution of flow variables at the flow/solid interface. The black band next to the panel in Fig. 4 indicates the high concentration of elements in the boundary layer near the panel. About 10 nodes in the vertical direction lie within the boundary layer. At the left and right ends of the panel, conduction heat transfer is permitted to the panel holder. Perfect condition contact is assumed. The bottom surface of the panel is assumed perfectly insulated.

The two cases of panel structural boundary conditions considered are shown in Fig. 4. In the first case, the panel is supported by immovable supports on the bottom corners as shown. For these boundary conditions and no temperature gradient through the panel thickness, the panel deforms into a convex shape. In the second case, the panel is supported by immovable supports at the top corners, and the panel deforms into a concave shape.

The flow/thermal/structural interaction for the flat plate was analyzed using the solution sequence shown in Fig. 6. The figure shows that panel deformations were computed three times at 10-s intervals for a test duration of 30 s. Calculations were also performed where the panel deformations were computed only once after a heating interval equal to the total test duration of 30 s. For convex deformations, the results for the two analysis sequences were in excellent agreement but, for the concave deformations, the results indicate that a smaller interval for deformation updates is required. The results to be presented in subsequent figures for the convex and concave deformations of the flat panel are for the analysis sequence shown in Fig. 6, i.e., three computations of panel deformations.

In a typical coupled flow/thermal analysis (*F/T* in Fig. 6), a time step of 1.E-7 s was used, and 4000 steps were required to approach steady heating rates in about 0.4 ms. In a typical thermal analysis (*T* in Fig. 6), a time step of 0.01 s was used, and 1000 steps were required to heat the panel for 10 s. A test duration of 30 s is early in the transient response of the panel; radiation equilibrium is estimated to occur after about 600–900 s of heating.

The interaction between the panel deformation and the flow density distribution is shown in Fig. 7 at three times, $t = 10, 20, 30$ s. The figure shows the development of a shock emanating from the left support on the windward side of the deformed panel. The fluid density increases through the shock, but the density decreases as the flow expands across the convex center of the panel along the leeward side toward the right support. As the flow is turned by the panel near the outflow, a recompression occurs, and the density begins to increase as a recompression shock is developed. As the panel deforms, the boundary-layer thickness is altered over the panel, becoming thinner on the windward surface and appreciably thicker on the leeward surface of the panel, as well as on the panel holder near the outflow.

The evolution of the temperature at the fluid/panel interface is presented in Fig. 8 for the panel with convex deformation. Because of the small Biot number of the panel, there is virtually no temperature gradient through the panel thickness, and the panel temperature varies only with x as shown. The "rounding" of the temperature distributions near the left and right panel supports is due to conduction heat transfer to the panel holder.

The heating rate for the panel with convex deformation is presented in Fig. 9. Figure 9a shows the evolution of the heating rate distribution as the panel deforms for $t = 0, 10, 20, 30$ s. The heating rate distribution displays the effects of both the fluid/panel heat transfer and the panel deformation. The overall decrease in the heating rate at each time is due to the rise of the panel temperature. Fluid temperatures (not shown) near the panel at each time remain roughly the same and, owing to the rise in the panel temperature, there is a lower temperature gradient at the fluid/panel interface that produces the lower heating rate. The panel deformation causes the increase in the heating rate distribution on the windward side of the panel for $1 < x < 2$.

The effect of the panel temperature on heating rate distribution is illustrated further in Fig. 9b. This figure compares the heating rate of a deformed panel, assuming a constant specified temperature, to the heating rate that occurs when the panel temperature is permitted to rise as in Fig. 8. The upper curve for the specified panel temperature shows the significant rise in heating rate for $1 < x > 2$, clearly demonstrating the deformation coupling effect.

The evolution of the thermal stress distributions on the top and bottom surfaces of the panel is presented in Fig. 10 for the convex deformation case. The panel experiences a large compression stress because longitudinal expansion is prohibited by the immovable supports. Because the supports are offset from the panel neutral surface, bending is superimposed, which produces small tensile stresses on the panel's top surface. The

Table 2 Panel temperature, $T(\ell/2,t)$, °R

t, s	Finite elements, Fig. 8	Analytical solution, Eq. (10)	Percent difference
10	595	599	0.7
20	650	665	2.3
30	705	729	3.3

Table 3 Panel deformation, $v(\ell/2,t)$, in.

t, s	Finite elements, Fig. 7	Analytical solution, Eq. (11)	Percent difference
10	0.0133	0.0127	4.7
20	0.0239	0.0234	2.1
30	0.0327	0.0336	2.7

Table 4 Panel stresses, $\sigma_x[(\ell/2), \pm (h/2), t]$, ksi

	$\sigma_x[(\ell/2), (h/2), t]$, ksi		$\sigma_x[(\ell/2), -(h/2), t]$	
t, s	Finite element, Fig. 10	Analytical solution, Eq. (13)	Finite element, Fig. 10	Analytical solution Eq. (13)
10	6.3	7.6	−14.7	−13.2
20	12.5	15.2	−26.7	−24.0
30	17.5	22.9	−36.3	−34.3

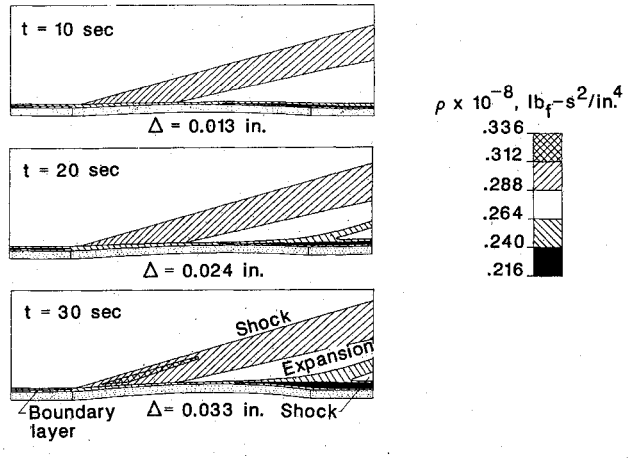

Fig. 7 Flow density distributions for panel with convex deformation.

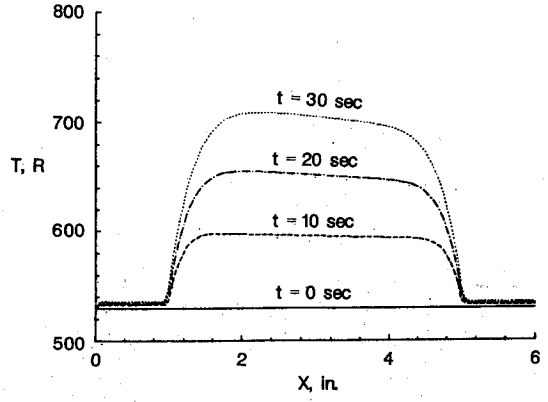

Fig. 8 Temperature distributions at fluid/panel interface for panel with convex deformation.

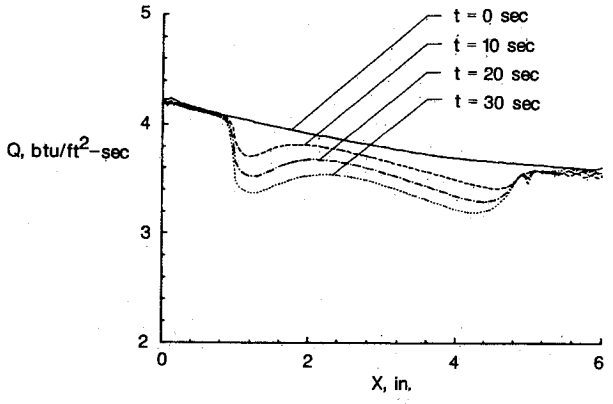

a) Evolution of heating rate distribution.

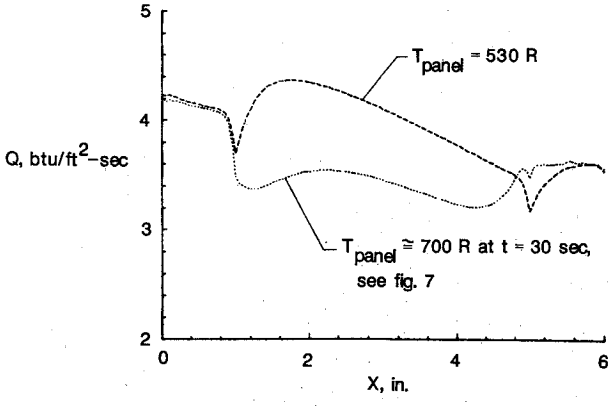

b) Effect of panel temperature on heating rate distribution.

Fig. 9 Heating rate distributions for panel with convex deformation.

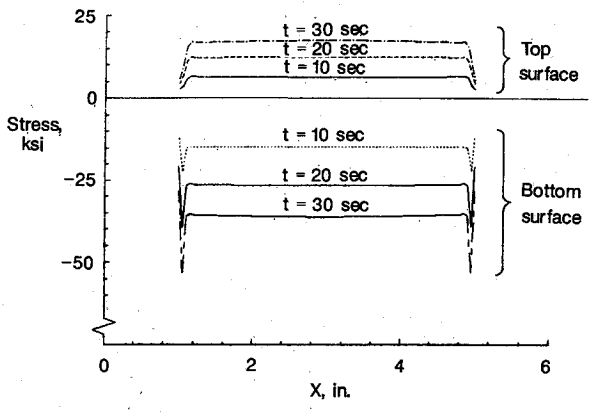

Fig. 10 Thermal stress distributions for panel with convex deformation.

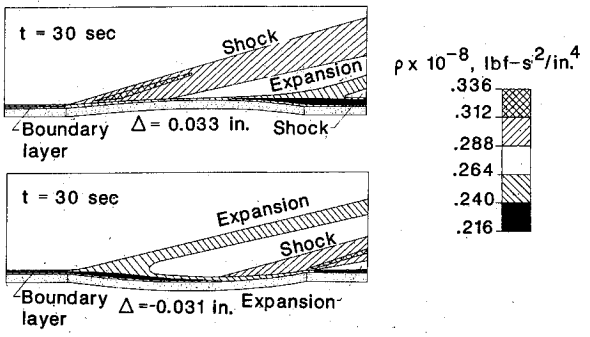

Fig. 11 Flow density distributions for panel with convex and concave deformations at 30 s.

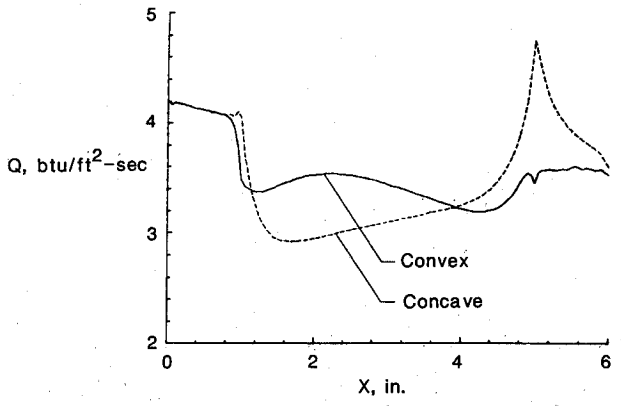

Fig. 12 Heating rate distributions for panel with convex and concave deformations at 30 s.

local oscillations in the bottom surface stresses at $x = 1$ and $x = 5$ are unrealistic and indicate the need for further mesh refinement in these areas.

The validity of the finite-element coupled flow/thermal/structural analysis was evaluated for the panel convex deformation using the approximate analytical solution presented in Eqs. (8–13). Panel temperatures, maximum deformation, and stresses are compared in Tables 2–4.

The results presented in the tables show that the approximate analytical solution agrees quite well with the finite-element solution for $10 \leq t \leq 30$. This agreement validates the finite-element approach and justifies application of this approach to cases for which the analytical approach is not applicable. The analytical solution is limited to thin elastic panels with uniform temperature. The finite-element approach is applicable to the more general practical structures depicted in Fig. 1.

The second case considers the supports at the top corners of the panel, producing concave deformation. The flow density distributions at $t = 30$ s for the panel with convex and concave deformations are compared in Fig. 11. The different deformations alter the flow significantly. In the concave case, an expansion occurs as the flow encounters the left support. The fluid density decreases through the expansion, but it begins to increase significantly as the flow turns through the bottom of the concave panel. Recompression occurs and a shock emanates from the right support. The boundary layer is altered differently for the two cases as well. For concave deformation, the boundary layer thickens after the flow encounters the left support, and then it thins as the flow approaches the right support. These differences in the flow are illustrated clearly by the heating rate distributions that are compared in Fig. 12 at $t = 30$ s. For the concave case, as with the convex case, there is an overall drop in heating rate owing to the rise in plate temperature. As a result of the strong recompression at the right support for the concave

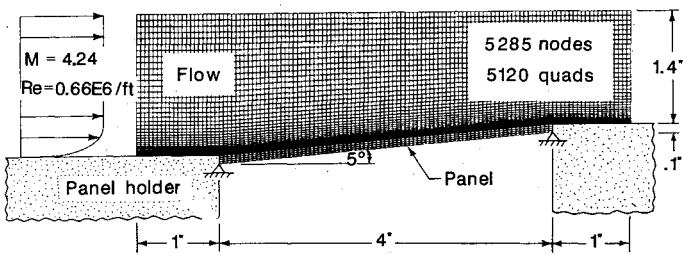

Fig. 13 Coupled flow/thermal/structural finite-element model and boundary conditions for flow over 5-deg panel.

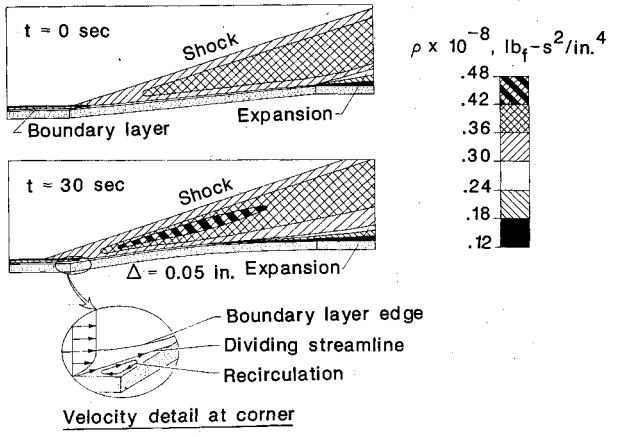

Fig. 14 Flow density distributions for 5-deg panel.

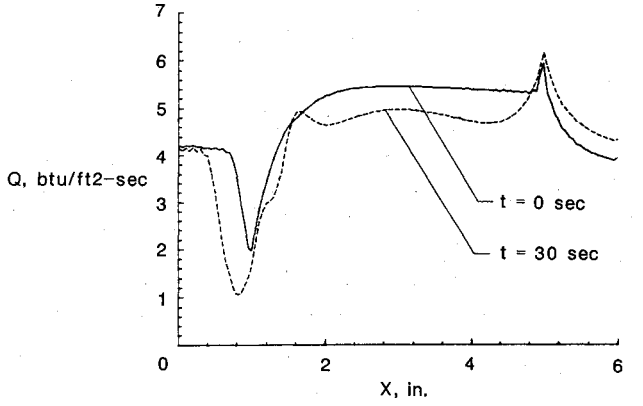

Fig. 15 Heating rate distributions for 5-deg panel.

case, however, there is a sharp rise in the heating rate above the flat plate near $x = 5$.

This example illustrates that flow/thermal/structural compling can significantly alter aerodynamic heating rates. Only very modest deformations occurred, but flow features were altered significantly. The location of the panel supports and the associated cases of convex and concave deformations caused the flowfields to differ considerably. Heating rate distributions changed markedly. In both cases, the simple initial boundary-layer flow was altered to produce much more complex flows, which can be predicated only by solving the full Navier-Stokes equations.

5-Deg Panel

The finite-element model and boundary conditions for the 5-deg panel are shown in Fig. 13. The model, boundary conditions, and solution procedure are identical to the flat panel application. The difference is that, in the undeformed state, the 5-deg panel presents a compression corner to the flow with a more complex initial flow, a more complex initial heating rate distribution, and higher local heating rates. The structural boundary conditions for the panel are located at the lower corners, causing convex deformation into the flowfield.

The effect of the panel deformation on the flow density distribution is shown in Fig. 14. Density distributions are compared for the undeformed panel and the deformed panel at $t = 30$ s. For the undeformed panel, a strong shock emanates from the compression corner at the left support, and the panel deformation makes the shock stronger. For the undeformed panel, an expansion occurs as the flow turns the "sharp" corner at the right support. The panel deformation makes the corner more rounded, however, and the expansion region moves upstream near the middle of the bowed panel. More significantly, for the undeformed panel, there is a small recirculation at the left support that becomes much larger as the panel deforms, giving a "stronger" compression corner. The recirculation region has a major effect on surface quantities such as skin friction and heating rate.

The heating rate distribution for the undeformed and deformed panel are compared in Fig. 15. The initial drop in heating rates at $x = 1$ is associated with the boundary-layer thickening and the onset of the flow separation as the flow approaches the corner. As the panel deforms, the flow separates farther upstream, giving a larger recirculation region, as indicated by the drop in heating rate at $x = 0.4$ in. for the deformed plate. As with the flat plate, an overall drop in the heating rate distribution results from the rise in plate temperature. The panel deformation, as before, significantly alters the heating rate distribution.

If the analysis were continued for longer times, the panel deformation would increase, and the recirculation region would grow in size until it reached the inflow boundary of the finite-element model. Then the analysis would become invalid. Thus, this problem demonstrates that the effect of the deformation on the flowfield must be given careful consideration in planning the computational domain.

Concluding Remarks

A finite-element approach for the coupling of flow, thermal, and structural analyses of aerodynamically heated panels is described. The paper brings together for the first time the solutions of the Navier-Stokes equation for high-speed compressible flow and of the associated thermal/structural equations by a single finite-element algorithm in one integrated vectorized program.

The approach is used to study flow, thermal, and structural interactions of two thin metallic panels proposed for an experimental study in the NASA Langley 8-ft HTT. Numerical results are presented that demonstrate the effect of the panel deformation and temperature on the flowfield and aerodynamic heating. For Mach 6.6 tunnel flow conditions, panel deformations alter the flow significantly. The panel deformations introduce shocks, expansions, and recirculation regions in the flow. Heating rate distributions are altered significantly. For the test durations studied (up to 30 s), the effect of the rising panel temperature is to lower overall heating rates. The effects of the convex panel deformations are to increase local heating rates on windward surfaces and decrease them on the leeward surfaces.

The coupling of the flow/thermal/structural analyses has provided insight into some of the fundamental features of interaction of supersonic/hypersonic flow with heated panels. Future analyses will focus on interactions on more realistic structures of current design interest, such as the leading edge of the scramjet fuel injection strut.

Acknowledgments

The first author is pleased to acknowledge the continuing support of the Aerothermal Loads Branch at the NASA Langley Research Center, and the advice and encouragement of the technical monitor, Dr. Allan R. Weiting.

References

[1]Shideler, J. L., Webb, G. L., and Pittman, C. M., "Verification Tests of Durable Thermal Protection System Concepts," *Journal of Spacecraft and Rockets*, Vol. 22, Nov.-Dec. 1985, pp. 598–604.

[2]Olsen, G. C. and Smith R. E., "Analysis of Aerothermal Loads on Spherical Dome Protuberance," *AIAA Journal*, Vol. 23, May 1985, pp. 650–656.

[3]Glass, C. E. and Hunt, L. R., "Aerothermal Test of Spherical Dome Protuberances on a Flat Plate at a Mach Number of 6.5," NASA TP-2631, Dec. 1986.

[4]Donea, J., "Taylor-Galerkin Method for Convective Transport Problems," *International Journal for Numerical Methods in Engineering*, Vol. 20, Jan. 1984, pp. 101–120.

[5]Bey, K. S., Thornton, E. A., Dechaumphai, P., and Ramakrishnan, R., "A New Finite Element Approach for Prediction of Aerothermal Loads – Progress in Inviscid Flow Computations," AIAA Paper 85-1533, July 1985; also NASA TM-86434.

[6]Thornton, E. A. and Ramakrishnan, R., "A Finite Element Approach for Solution of the 3D Euler Equations," AIAA Paper 86-0106, Jan. 1986.

[7]Thornton, E. A., Dechaumphai, P., and Vermaganti, G., "A Finite Element Approach for Prediction of Aerothermal Loads," AIAA Paper 86-1050, May 1986.

[8]Thornton, E. A. and Dechaumphai, P., "A Taylor-Galerkin Finite Element Algorithm for Transient Nonlinear Thermal-Structural Analysis," AIAA Paper 86-0911, May 1986.

[9]Cook, R. D., *Concepts and Applications of Finite Element Analysis*, Wiley, New York, Jan. 1984, pp. 296–297.

[10]Lapidus, A., "A Detached Shock Calculation by Second-Order Finite Difference," *Journal of Computational Physics*, Vol. 2, Nov. 1967, pp. 154–177.

[11]Zienkiewicz, O. C. and Lohner, R., "Accelerated Relaxation or Direct Solution? Future Prospects for FEM," *International Journal for Numerical Methods in Engineering*, Vol. 21, Jan. 1985, pp. 1–11.

[12]Boley, B. A. and Weiner, J. H., *Theory of Thermal Stresses*, Wiley, New York, March 1960, pp. 411–418.